Collapse of a rectangular well in a quasi-two-dimensional granular bed

Simon J. de Vet,[1,2,*] Bereket Yohannes,[3,†] K. M. Hill,[3,‡] and John R. de Bruyn[1,§]
[1]*Department of Physics and Astronomy, University of Western Ontario, London, Ontario, Canada N6A 3K7*
[2]*Department of Physics and Atmospheric Science, Dalhousie University, Halifax, Nova Scotia, Canada B3H 3J5*
[3]*St. Anthony Falls Laboratory, Department of Civil Engineering, University of Minnesota, Minneapolis, Minnesota 55414, USA*
(Received 9 June 2009; revised manuscript received 7 September 2010; published 21 October 2010)

We report on an experimental and numerical study of the collapse under gravity of a rectangular well in a quasi-two-dimensional granular bed. For comparison, we also perform experiments on the collapse of a single vertical step. Experiments are conducted in a vertical Hele-Shaw cell, which allows the flow to be recorded from the side using high-speed video. If the rectangular well is sufficiently narrow, the collapsing sidewalls collide at the center of the well and the dynamics of the collapse are dependant on the aspect ratio of the initial well. We follow the evolution of the free surface from the video images, and use particle image velocimetry to determine the subsurface velocity field. From these data, the potential and kinetic energy of the system are calculated. We observe two stages to the collapse flow: an initial gravity-dominated stage, during which the kinetic energy increases, and a later dissipation-dominated phase during which the kinetic energy decreases. We find that although both the width and depth of the depression that remains after the well has collapsed depend on the initial aspect ratio, the surface profiles are self-similar; that is, the shape of the final profile is independent of the aspect ratio of the initial well. We model the collapse of the well using a depth-averaged continuum model with basal friction and with a discrete element model. Both models give results which agree well with experiment. The discrete element model indicates that friction between the particles is the most important source of dissipation over the course of the collapse.

DOI: 10.1103/PhysRevE.82.041304 PACS number(s): 45.70.Cc, 45.70.Ht, 47.15.gp

I. INTRODUCTION

Dense granular materials are capable of supporting a nonzero shear stress, both in the bulk and at the free surface. In a gravitational field there is therefore a maximum free surface slope known as the repose slope α, below which the granular system does not spontaneously flow. When the repose slope is exceeded, the surface becomes unstable and a flow is initiated, driving the system back toward a metastable configuration. A tiny perturbation on an otherwise stable slope may grow into a large avalanche. A system very far from stability—one with an initially vertical step, for example [1–6]—will spontaneously collapse, resulting in a transient granular flow as the system evolves toward a metastable final configuration. This is the scenario we study in this paper. In particular, we investigate the nature of this transient flow and how it determines the shape of the final metastable state.

The steady flow of granular materials down a slope has been studied in some detail [7,8], and theoretical descriptions of dense granular flows that have some degree of generality have been proposed [9–12]. The collapse of a granular step or column is more complex, however, in part because the flow is transient and its nature changes dramatically with time [3,13].

The collapse of a vertical granular step, known as the granular dam-break problem, has been the subject of several recent experiments [1–6]. It has been observed that a relatively thick region of material initially falls more-or-less vertically. The system quickly evolves into a thin flowing layer at the free surface as the material spreads horizontally [1,3,6]. The flow eventually comes to rest when the initial gravitational potential energy has been dissipated by friction and collisions among the particles. The final profile of the granular material has been observed to have a linear segment with a slope close to the repose slope and a curved tail at its base [2,3]. The two-sided collapse of rectangular columns of granular material and the axisymmetric collapse of cylindrical columns have also been the subject of recent experiments [1,14–17]. These problems have also been attacked theoretically, using continuum models [1,2,13,18,19], discrete element simulations [6,20–22], and finite element calculations [23]. While progress has been made toward understanding this family of granular flows, fundamental questions remain about the role of friction and the best way to model it [1,13,16,20], and it remains to be seen how well current models of granular rheology [11,12] apply to these systems [22].

Recently we [24–26] and others [27–33] have studied the formation of impact craters by a projectile falling into a granular material. It is believed that the shape of a (much larger) planetary impact crater is determined by the collapse of an unstable transient crater excavated by the impact of a projectile [34], and it is reasonable to assume that a similar process is at work in the case of low-energy impacts in a granular bed. Although the geometry is slightly different from previously studied cases, this is another example of the relaxation of a highly unstable initial granular configuration toward some final metastable state. In this paper we study a simplified version of this problem in an effort to gain insight into the collapse of the transient crater without the substan-

*sdevet@dal.ca
†tewol002@umn.edu
‡kmhill@umn.edu
§debruyn@uwo.ca

tial added complication of the impact. We investigate the collapse of an initially rectangular well of depth D and width W in a vertical Hele-Shaw cell. For comparison, we also study the collapse of an isolated vertical step of height D in the same experimental apparatus. The collapse is recorded using high-speed video. Individual video frames are digitally processed to extract the profile of the free surface as a function of time, and particle image velocimetry [35] is used to measure subsurface flow fields.

At the earliest stages, there is no difference between the collapse of a single isolated step and the collapse of each side of a rectangular well. If the rectangular well is sufficiently narrow, however, the collapsing walls will collide at its center. From this point on, the collapsing walls no longer behave as isolated steps, and the dynamics become dependent on the aspect ratio of the initial well. After the collision of the walls, the evolution of the system slows and the well fills. We find that while the size of the final profile depends on the aspect ratio of the initial well, its shape does not.

To investigate the role of friction in the system dynamics, we also model the collapse of a rectangular well using two techniques: a continuum model based on the shallow-layer Saint-Venant equations with a simple basal friction term [2,13,19,36] and a discrete element model [20–22,37,38]. Both models reproduce the key features seen in the experimental system. Despite the simplicity of the former model, we find near-quantitative agreement with our experimental results with all parameters constrained by experiment. The discrete element model shows a similar level of agreement with experiments, and also allows us to extract detailed information about the dissipation processes at play during the flow.

II. EXPERIMENT

We conduct our experiments in a vertical Hele-Shaw cell, depicted schematically in Fig. 1. Two panes of transparent glass, $70\times70\times1$ cm^3 are held vertically in a rigid metal frame, with a gap of $a=0.47$ cm between them. The gap width is held fixed in our experiments.

We use nearly monodisperse spherical glass beads with a density $\rho_g=2500$ kg/m^3 and a diameter of 0.78 ± 0.01 mm as our granular medium [39]. To introduce contrast for imaging, red and white beads (as purchased from the supplier) are mixed at a 5:1 ratio. We could not discern any differences in the friction coefficient, angle of repose, or other properties of the red and white beads. The beads are poured into the apparatus from above. The packing fraction of the beads in the cell is difficult to measure directly because of small variations in the cell width. However, recent numerical results on the packing of spheres in confined geometries have shown that the packing fraction is independent of the gap width a when the ratio $a/r_b\gtrsim10$, where r_b is the bead radius. In our case $a/r_b\approx12$, so we assume that the beads are randomly packed with a packing fraction of 0.61 ± 0.01, the value measured by pouring the beads into a beaker. This corresponds to a bulk granular density of $\rho_v=1530\pm20$ kg/m^3. Within the cell, the mass per unit area is therefore $\rho_a=7.19\pm0.09$ kg/m^2. We observed no electrostatic effects between the glass walls and the glass beads during filling or experiments.

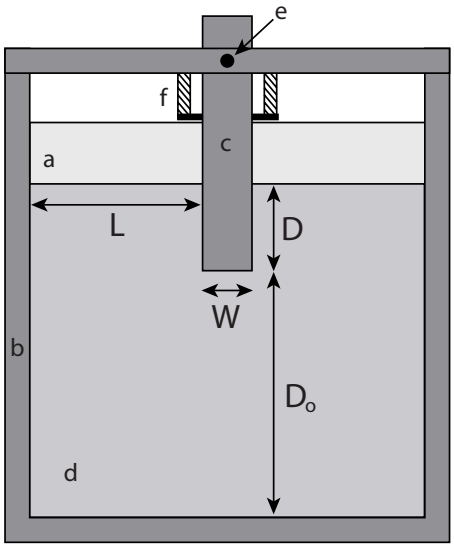

FIG. 1. (Color online) A schematic view of the experimental apparatus (not to scale). Two glass panes (a) are held in a metal frame (b) with a 4.7 mm gap between them. An acrylic barrier of width W and 4.7 mm thickness (c) is lowered into the gap, and the cell is filled with spherical glass beads (d) as described in the text. To initiate an experiment, a restraining pin (e) is removed, and springs (f) cause the barrier to be quickly pulled up and out of the granular bed.

If the beads are poured into the cell and then allowed to drain slowly through a single hole in the bottom [40], we find that they achieve a repose slope of $\alpha=0.5008\pm0.0004(26.60\pm0.02°)$. This is significantly higher than the slope of $0.46\pm0.01(24.8\pm0.5°)$ found when the beads are unconfined and allowed to drain freely in three dimensions. This suggests that the interactions between the beads and the sidewalls increase the stability of the pile, as has been noted in previous experimental studies [41–44] and simulations [45]. The slope is measured directly in the two-dimensional (2D) experiments, but calculated indirectly in three-dimensional 3D [46], hence the significant difference in precision.

The cell is completely drained prior to every experiment. The lower edge of the cell is sealed, and the cell is filled to a uniform depth D_o by slowly pouring the glass beads from above. A rectangular acrylic barrier of width W and a thickness sufficient to completely fill the gap is lowered into the cell, applying tension to a pair of springs, so that its lower surface is flush with the upper surface of the granular bed. The barrier is held in place with a restraining pin. For the single-step configuration, additional beads are added on one side of the barrier to a height D above the bottom of the barrier. For the rectangular well, additional beads are added on both sides of the barrier.

To begin the experiment, the restraining pin is removed and the springs pull the barrier upward with an acceleration of nearly 250 m/s^2. The time required for the barrier to be extracted (0.02 s for $D=5$ cm, our greatest depth) is small compared to the time required for the beads begin flowing

under gravity. We observed that very little upward momentum is imparted to the granular bed by the barrier. Following the removal of the barrier, the beads are essentially at rest and form either a single vertical step of height D or a rectangular well of depth D and width W.

The vertical walls immediately begin to slump under gravity. The collapse is recorded using a high speed charge coupled device (CCD) camera (Motion Scope PCI 1000S, Redlake Imaging Corp.), triggered by the initial upward motion of the barrier. Images are collected at 500 frames per second, in 256-level greyscale, at a resolution of 320 $\times 280$ pixels. The cell is illuminated by lights positioned to avoid glare or reflections from the glass walls or the beads themselves. The spatial resolution of the images in physical units changes from experiment to experiment, as the field of view of the camera is adjusted to best capture the entire subsurface flow. The resolution is not sufficient to resolve individual beads, but small regions containing more or fewer white beads can be distinguished and tracked as described below.

Four different barriers of width $W=1.27$, 2.54, 5.08, and 10.16 cm are used to create the wells. For each value of W, measurements are made for ten burial depths, from $D=0.5$ cm to $D=5$ cm in 0.5 cm intervals. Two experiments are performed for each possible width-depth pair. In every case the width and depth of the initial well are at least an order of magnitude smaller than the width and depth of the cell, respectively. We therefore avoid system-size effects. The thickness of the gap is small compared to the size of the well, and high-speed video recordings taken from above confirm that there is no significant flow perpendicular to the plane of the cell. The flow in our system is therefore quasi-two-dimensional. Furthermore, the dimensions of the initial well are large compared to the size of the individual glass beads, and we see no evidence of bead-size effects in our experimental results.

The profile of the upper free surface of the granular material, $h(x)$, is obtained from each video frame using an edge detection routine, after first applying a smoothing filter to reduce image noise. Defining $h=0$ at the bottom of the initial well and using the mass per unit area ρ_a, we calculate the gravitational potential energy P of the system as

$$P = \frac{1}{2}\rho_a g \int h^2(x)dx, \tag{1}$$

where g is the acceleration due to gravity.

Particle image velocimetry (PIV) is used to measure the subsurface velocity field [35]. PIV methods use cross-correlations between consecutive video frames to determine local velocities [47]. In our case, we do not use the motion of individual particles to calculate the velocities, but rather the displacement between successive video frames of local arrangements of red and white beads [35]. The kinetic energy K_t associated with the translation of the beads is calculated from the resulting velocity field. The accuracy of the flow fields and hence the kinetic energy calculation is limited by the resolution of our images. In particular, it is difficult to determine the flow field accurately when the flowing layer is thin.

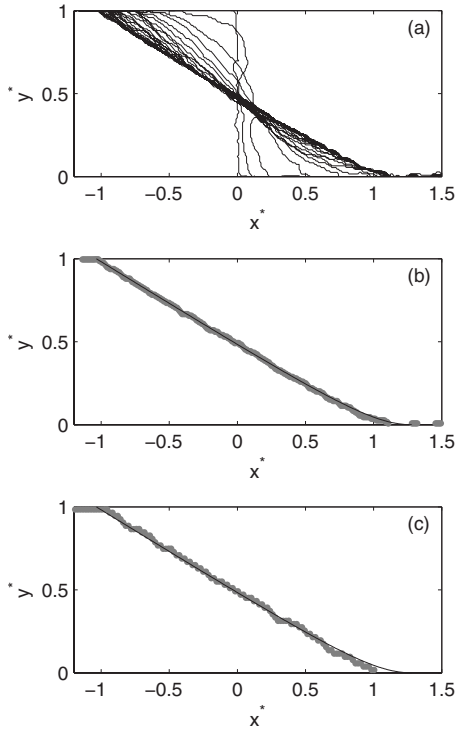

FIG. 2. (a) The evolution of the free surface for a 5 cm deep dam-break. Profiles are plotted at $\Delta t^*=0.4$ ($\Delta t=0.028$ s) intervals. The original step is located at $x^*=0$. (b) A fit of the late-time profile (gray points) to a half-hyperbola (solid line) given by Eq. (3). (c) shows the final profile and corresponding fit for a 2.5 cm deep dam break.

III. EXPERIMENTAL RESULTS

A. Single step ("dam-break")

We first investigate the collapse of a single step. Previous work on granular collapse has emphasized the dependence of the final configuration of the system on its initial aspect ratio [1–3,14–17], that is, the ratio of the step height D to the width of the top of the step (L in Fig. 1) or the width of the granular column, as appropriate. In our single-step experiments, the system is sufficiently wide that the flow never extends to the boundary and this aspect ratio is effectively zero. In this case, the only relevant length scale is the original step height D. We therefore characterize the system using dimensionless lengths $x^*=x/D$ and $y^*=y/D$, and dimensionless time $t^*=t/\sqrt{D/g}$. (Throughout this paper, the superscript $*$ notation indicates dimensionless quantities.) We define $t^*=0$ at the moment when the acrylic barrier has completely cleared the upper surface of the bed, $x^*=0$ at the edge of the single step, and $y^*=0$ at its base.

The evolution of the upper free surface of a collapsing step with $D=5.0$ cm is shown in Fig. 2(a). At the earliest times, the base of the vertical wall begins to spread outward while a portion of the originally horizontal upper surface tilts downward. By $t^*\approx 1.0$ the original corner has become suffi-

ciently rounded that the distinction between these two surfaces vanishes. At $t^* \approx 2.0$ the surface is very close to the repose slope everywhere, but the flow does not completely terminate until $t^* \approx 5.5$. In their dimensionless form, the late-time profiles are the same for all experiments, independent of D. This is seen by comparing Figs. 2(b) and 2(c), which show the final profiles for steps with $D=5$ and 2.5 cm. These results are consistent with previous work [1–6].

We fit the shape of the final profile to the empirical form

$$x^* = ay^* - b \ln y^* + x_0^*. \tag{2}$$

proposed in Ref. [3], consisting of a linear profile with a logarithmic tail at its leading edge. Simultaneously fitting to the late-time profiles from all of our runs, we find $a=-1.992 \pm 0.008$, $b=0.050 \pm 0.002$, and $x_0^*=0.944 \pm 0.006$, nearly identical to those reported in [3].

Recently, we reported that the profiles of impact craters formed in a granular target were well described by hyperbolae [26]. With this in mind, we fit the late-time profile formed by the collapse of a single step to half a hyperbola, given by

$$y^* = y_c^* + \sqrt{(y_c^*)^2 + c^2(x^* - x_0^*)^2}. \tag{3}$$

Unlike Eq. (2), for which $x=\infty$ at $y=0$, the rounded tail of the half-hyperbola is finite in extent. Simultaneously fitting to all experimental late-time profiles, we find $y_c^*=-0.20 \pm 0.01$, $c=0.511 \pm 0.002$, and $x_0^*=1.28 \pm 0.01$. This fit is shown in Figs. 2(b) and 2(c). While Eq. (3) provides a slightly better fit to the data than Eq. (2), the two fits are virtually indistinguishable to the eye.

Figure 3 shows the granular flow field during the collapse of a step with $D=5$ cm. At the earliest times the flow lines are curved, connecting the vertical wall to the horizontal upper surface. The boundary between the flowing and static regions is sharp [4]. By $t^*=1$ the flow lines have become quite straight. The flowing region becomes thinner as time progresses until the flow terminates completely, as observed previously [1,3,16].

From the measured free surface profiles and flow fields, we calculate the potential and kinetic energies of the system as a function of time, as described above. We define the dimensionless potential energy as $P^*=P/E_0$ and the dimensionless kinetic energy as $K_t^*=K_t/E_0$, where $E_0=(1/2)\rho_a g D^3$, and we measure changes in P^* relative to its value at $t^*=0$.

The energies calculated for the collapse of a step with $D=5$ cm are shown in Fig. 4. The potential energy decreases monotonically over the course of the collapse, approaching a constant value at late times. The kinetic energy, on the other hand, increases at early times, reaching a maximum at $t^* \approx 0.5$. K_t^* then decreases, eventually going to zero. This suggests that the flow can be divided into two phases: the first phase of the flow is dominated by the conversion of gravitational potential energy into kinetic energy, while the second phase is dominated by dissipation processes. The transition from one phase to the other is gradual, and occurs at roughly the same time as the transition from curved flow lines to straight flow lines parallel to the upper free surface.

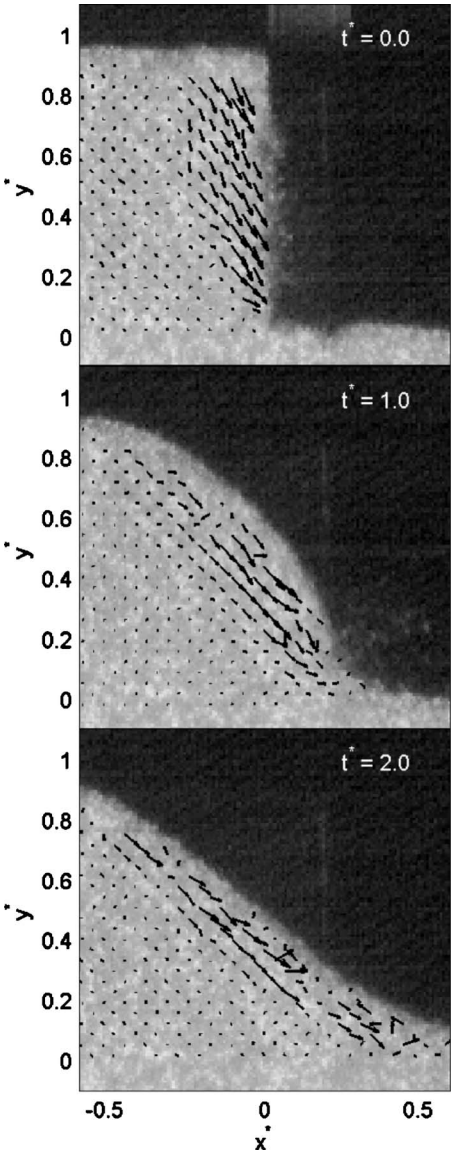

FIG. 3. Subsurface flow field during the collapse of a single vertical step with an initial height of $D=5$ cm. Flow fields are shown at early ($t^*=0$), intermediate ($t^*=1$), and late ($t^*=2$) times. For clarity, only one in four calculated velocity vectors is shown.

B. Rectangular well

The free surface of a collapsing rectangular well with $D=5$ cm and $W=5.08$ cm is shown for several times in Fig. 5(a). In this case, we define $x^*=0$ at the center of the initial well and $y^*=0$ at its base. Before the walls collide at the center of the well, they each behave as a collapsing single step. The dynamics change after the walls collide. In some cases, the collision of the walls is sufficiently violent that a small central peak is formed, as seen in one of the profiles plotted in Fig. 5(a). This is analogous to the formation of granular jets in impact experiments [30,48]. These peaks, when present, form shortly after the walls collide but are erased by subsequent flow and not found in the late-time profiles. When the flow has terminated, the depth of the profile at $x^*=0$ is shallower than the initial well.

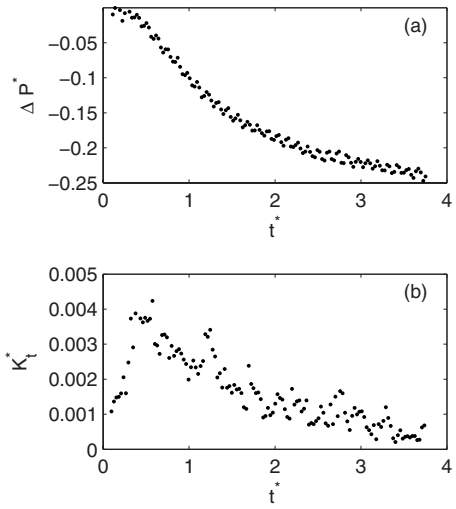

FIG. 4. The dimensionless energy for the collapse of a step with $D=5$ cm. (a) The dimensionless change in potential energy ΔP^* as a function of dimensionless time t^*. (b) The dimensionless kinetic energy K_t^* as a function of t^*.

The behavior of a collapsing rectangular well depends on its initial aspect ratio $W^*=W/D$. Figure 6 shows the depth of the profile at $x^*=0$ as a function of time for several values of W^*. The depth of the well does not change prior to the collision of the walls. Following the collision, the well begins to fill and smoothly approaches the final depth. When W^* is small, the steps collide earlier, the well fills at a higher rate, and the final profile is shallower than for wells with larger aspect ratios. When $W^* \gtrsim 3$, the well is sufficiently wide that the flow stops before the walls collide. In this case, the walls always behave like independent steps, and the dynamics are independent of W^*.

We find that the depth $y^*_{\min}$ of the profile at the center of the well, shown in Fig. 6, can be well described by an exponential approach to a late-time depth following an initial delay, i.e.,

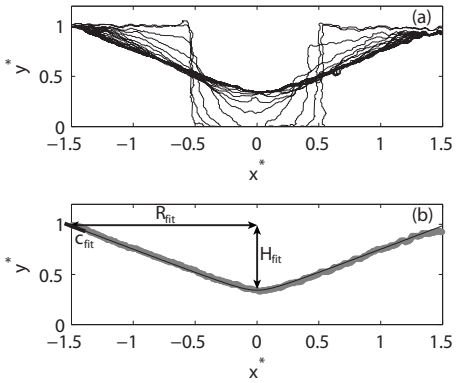

FIG. 5. (a) The evolution of the free surface for a $D=5$ cm, $W=5.08$ cm rectangular well. Profiles are plotted at $\Delta t^*=0.4(\Delta t=0.028$ s) intervals. (b) A fit of the late-time profile (gray points) to a hyperbola (solid line) given by Eq. (5). The radius and depth of the profile derived from the fit, $R_{\rm fit}$ and $H_{\rm fit}$ respectively, and the slope of the profile $c_{\rm fit}$ are also shown.

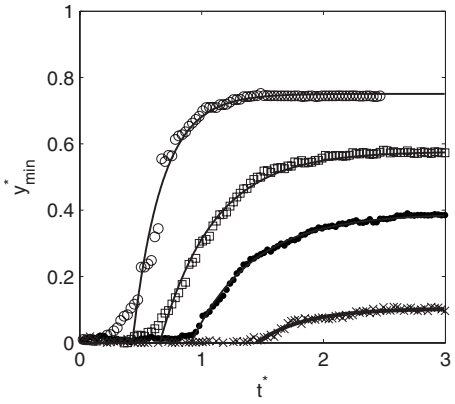

FIG. 6. The depth $y^*_{\min}$ at the center of the collapsing well as a function of dimensionless time t^*. ○ represent $W^*=0.25$, □ are $W^*=0.5$, ● are $W^*=1.0$ and × are $W^*=2.0$. All wells are of initial depth $D=5$ cm. The floor of the original well corresponds to $y^*=0$, and the original upper surface to $y^*=1$. Solid lines are fits to an exponential approach to the final depth, as given by Eq. (4).

$$y^*_{\min}(t^*) = \begin{cases} 0 & \text{if } t^* \le t^*_{start} \\ y^*_f(1-e^{-(t^*-t^*_{start})/t^*_{fill}}) & \text{if } t^* \ge t^*_{start} \end{cases}. \quad (4)$$

Fits of this function to the experimental data are shown in Fig. 6. The parameters in Eq. (4) have direct physical interpretations. t^*_{start} is the time at which the collapsing walls collide and the well begins to fill. t^*_{fill} is the time scale associated with the exponential approach to the final depth y^*_f, and is therefore a measure of the duration of the filling flow. As described by Eq. (4), the onset of filling is abrupt. Experimentally it is more gradual, reflecting the fact that the advancing front of the collapsing walls are not sharp, but the data approach the fit function on a time scale much smaller than t^*_{fill}.

Plots of the parameters determined from fits of our data to Eq. (4) are shown in Fig. 7. The collision time t^*_{start}, shown in Fig. 7(a), increases with increasing W^*. The time scale t^*_{fill} is plotted in Fig. 7(b). It is roughly constant with a value of 0.4 ± 0.1 for $W^* \lesssim 1$, but decreases for larger W^*. The dimensionless filling rate at $t^*=t^*_{start}$ is y^*_f/t^*_{fill}. As shown in Fig. 7(c), this quantity decreases with increasing W^*. When $W^* \gtrsim 3$ the walls do not collide, the depth of the well remains unchanged, and these quantities are all therefore undefined.

The late-time free surface profiles are fit to a hyperbolic function with a flat bottom, given by

$$y^*(x^*) = \begin{cases} y^*_c + \sqrt{(b^*)^2 + c^2(x^*+x^*_f)^2} & \text{if } x^* \le -x^*_f \\ y^*_c + b^* & \text{if } -x^*_f < x^* < x^*_f \\ y^*_c + \sqrt{(b^*)^2 + c^2(x^*-x^*_f)^2} & \text{if } x^* \ge x^*_f \end{cases}. \quad (5)$$

This is a two-sided version of Eq. (3), allowing for the presence of a flat bottom of half-width x^*_f. c is the asymptotic slope, b^* is a measure of the roundness of the hyperbola, and y^*_c is a vertical offset. If $x^*_f=0$, Eq. (5) describes a simple hyperbola. As well as being a generalization of the form used to describe the profile following the collapse of a single step,

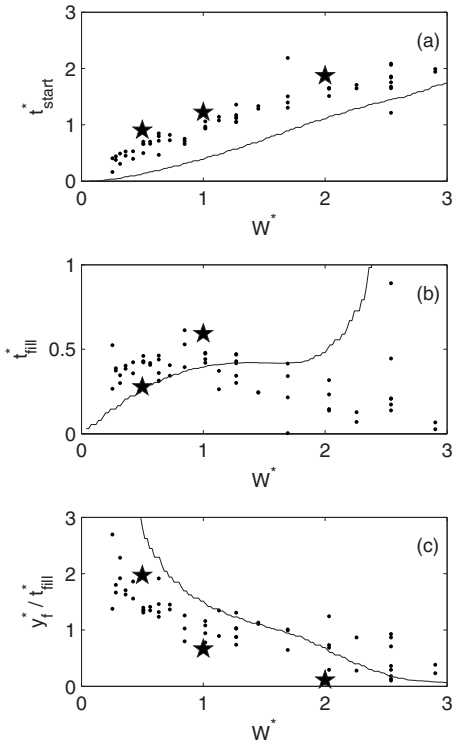

FIG. 7. The timing of the filling process as a function of the initial aspect ratio. (a) shows t_{start}, the time at which the well begins to fill. (b) shows t_{fill}, the time constant associated with the exponential approach toward the final depth. (c) shows the initial filling rate. In each plot the dots are the experimental data, the solid line is the prediction of the Saint-Venant model, and the stars are results obtained from the discrete element simulations.

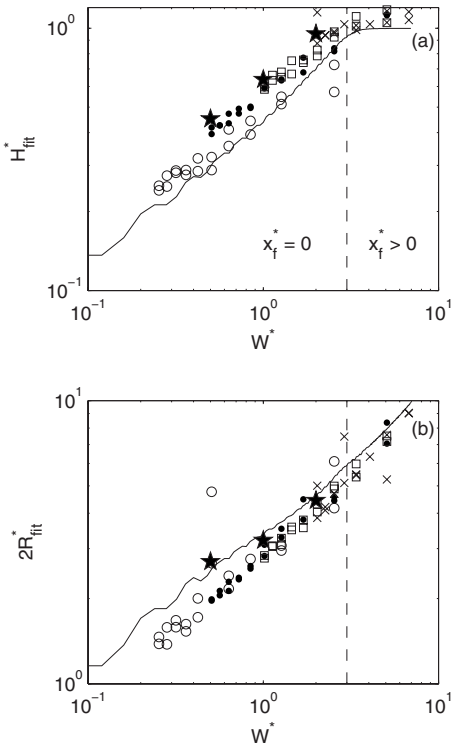

FIG. 8. The dimensionless depth (a) and width (b) of the final profile as a function of the initial aspect ratio of the rectangular well. In both plots ○ are experimental data for $W=1.27$ cm, ● for $W=2.54$ cm, □ for $W=5.08$ cm, and × for $W=10.16$ cm. Above $W^*\approx 3$, indicated by the dashed line, the collapsing walls do not interact. The solid line is the prediction of the Saint-Venant model, and stars are results obtained from profiles generated by the discrete element simulation.

the hyperbola is also the observed shape of impact craters in granular media [26]. Only the lower three-quarters of the experimental profile is fit to Eq. (5), since the experimental profiles deviate from the hyperbolic shape and approach $y^*=1$ at large x^*. We find that the profiles are well described by a simple hyperbola with $x_f^*=0$ when $W^*\lesssim 3$, but have a flat bottom when $W^*\gtrsim 3$, in which case the walls do not collide and a portion of the initially flat bottom remains unperturbed.

The late-time profile depth, measured from the original surface at $y^*=1$ to the lowest point, is given by $H_{\rm fit}^*=1-(y_c^*+b^*)$. Extrapolating the fitted hyperbolic profile to the original surface at $y^*=1$ gives the width of the profile as $2R_{\rm fit}^*=2[\sqrt{(1-y_c^*)^2-(b^*)^2}/c+x_f^*]$, and the extrapolated slope at the upper surface is given by $c_{\rm fit}=c\sqrt{1-(b^*)^2/(1-y_c^*)^2}$. These three dimensions are indicated on the profile plotted in Fig. 5(b).

$H_{\rm fit}^*$ is shown as a function of the initial aspect ratio in Fig. 8(a). For $W^*\gtrsim 3$ the center of the well never fills, so $H_{\rm fit}^*=1$. For $W^*\lesssim 3$, $H_{\rm fit}^*$ increases with increasing W^*. The dependence on W^* is well described by a power-law, with $H_{\rm fit}^*=(0.55\pm 0.01)W^{*(0.58\pm 0.03)}$. The profile width $2R_{\rm fit}^*$ is shown as a function of W^* in Fig. 8(b). It increases continuously with increasing initial aspect ratio; no significant change in behavior is seen at $W^*\approx 3$. Fitting these data to a power-law gives $2R_{\rm fit}^*=(2.84\pm 0.02)W^{*(0.52\pm 0.01)}$. The extrapolated slope does not depend on W^* and has a mean value of $c_{\rm fit}=0.47\pm 0.06$. This is equal, within uncertainties, to the repose slope of the confined granular medium.

All three parameters—$H_{\rm fit}^*$, $R_{\rm fit}^*$, and $c_{\rm fit}$ (or equivalently, y_c^*, b^*, and c)—are required to describe the final profile. However, the *shape* of the profile can be described by considering only its aspect ratio $R_{\rm fit}^*/H_{\rm fit}^*$ and the maximum slope $c_{\rm fit}^*$. Both $H_{\rm fit}$ and $R_{\rm fit}$ vary with W^*, but since they have nearly the same dependence on W^* for $W^*\lesssim 3$, the aspect ratio of the final profiles is nearly independent of W^*. As noted above, the maximum profile slope is also independent of W^*. As a result the profiles are self-similar; their shape is essentially independent of the aspect ratio of the initial well.

Figure 9 shows the subsurface flow field measured during the collapse of a square well with $W=5.08$ cm and $D=5.0$ cm. Prior to the collision of the walls, the flow on each side of the well is identical to that observed during the collapse of a single step. After the collision, velocities in the center of the well drop to zero. Thin surface flows which resemble those of the late stage dam-break persist outside of this central quiet zone.

Figure 10 shows the energy of the collapsing well as a function of time. As in the collapse of a single step, there are two phases to the flow. At early times, the kinetic energy K_t^* increases, again reaching a maximum value near $t^*=0.5$. At later times dissipation becomes more important, and the kinetic energy decreases toward zero. The potential energy decreases continuously throughout the entire collapse.

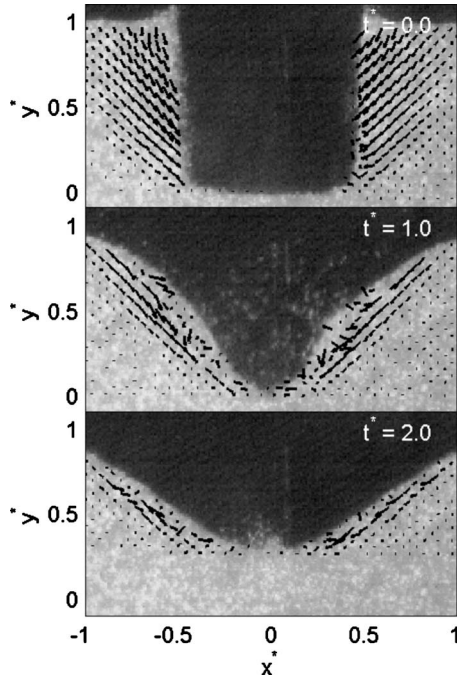

FIG. 9. Subsurface flow field during the collapse of a rectangular well with $D=5$ cm and $W=5.08$ cm. Flow fields are shown at early ($t^*=0$), intermediate ($t^*=1$), and late ($t^*=2$) times. For clarity, only one in four calculated velocity vectors is shown.

The evolution of the potential energy depends on the initial aspect ratio W^*. Prior to the collision, ΔP^* has no dependence on W^*. When the walls collide, the rate of change of ΔP^* decreases and ΔP^* approaches some final value. When W^* is small, the collision occurs earlier and the net change in potential energy is smaller. The kinetic energy is already small at the moment of collision, and we are unable to resolve any change in behavior at this point.

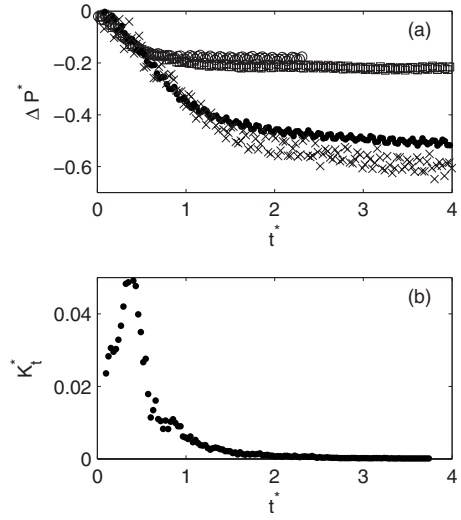

FIG. 10. The dimensionless energy for the collapse of a rectangular well. (a) The dimensionless change in potential energy ΔP^* as a function of dimensionless time t^*. ○ represent $W^*=0.25$, □ are $W^*=0.5$, ● are $W^*=1.0$ and × are $W^*=2.0$. All wells are of initial depth $D=5$ cm. (b) The dimensionless kinetic energy K_t^* as a function of t^* for a $W^*=1$ well.

IV. CONTINUUM MODEL

Following previous studies [13,19,36], we model the collapse of a rectangular well using the Saint-Venant equations for a shallow flowing layer, presented below. This model reduces the two-dimensional flow in our collapsing well to a one-dimensional problem by considering only the depth $h(x,t)$ of the granular bed as measured from the bottom of the initial well and the depth-averaged horizontal velocity $\bar{v}(x,t)$. The differential equations for h and $\bar{v}$ are [13]

$$\frac{\partial h}{\partial t}+h\frac{\partial \bar{v}}{\partial x}+\bar{v}\frac{\partial h}{\partial x}+D_h\frac{\partial^2 h}{\partial x^2}=0 \tag{6}$$

and

$$h\left(\bar{v}\frac{\partial \bar{v}}{\partial x}+\frac{\partial \bar{v}}{\partial t}\right)+gh\frac{\partial h}{\partial x}+fgh\frac{\bar{v}}{|\bar{v}|}+hD_v\frac{\partial^2 \bar{v}}{\partial x^2}=0. \tag{7}$$

Equation (6) is derived from conservation of mass, assuming that the granular medium is incompressible. Equation (7) is derived from conservation of momentum. The second term of Eq. (7) corresponds to a gain in momentum due to gravity as the granular material flows downhill, while the third term represents momentum loss, here modeled using a basal friction term [13] with an effective coefficient of friction f, which we assume to be constant. This term is intended to incorporate all dissipation processes, including both particle-particle and particle-wall interactions, using a single parameter; this is discussed further in Section VI. Equations (6) and (7) include diffusion terms with effective diffusion coefficients D_h and D_v, respectively. These are included to prevent the formation of sharp unphysical features in the depth or velocity profile.

We express Eqs. (6) and (7) in the same dimensionless form used in the experiments by setting $g=1$ and always using a well with an initial depth of $D=1.0$. The equations are integrated numerically on a regular grid with a spatial resolution of $\Delta x^*=0.02$, using an Euler update scheme with a constant time step of $\Delta t^*=1.6\times10^{-3}$. We confirmed that reducing the time step did not change the results. The model is integrated until $\bar{v}^*=0$ everywhere.

The dissipation parameter f is determined uniquely by the experimentally measured angle of repose. In this model, momentum is gained at a rate proportional to the local slope, and lost at a rate proportional to f. A steady state is achieved when gravity and dissipation are in balance, which occurs when the local slope is equal to f. We therefore set f equal to 0.5, the experimentally measured repose slope.

The dimensionless diffusion coefficients D_h^* and D_v^* do not have a simple physical interpretation, as diffusion within a flowing granular medium is complex and highly dependent on the local conditions [49]. The model dynamics show some dependence on the choice of D_h^* and D_v^*, particularly close to the moment when the two collapsing walls collide. The shape of the final profile, however, is nearly independent of this choice. For example, the depth of the final profile changes by less than 10% when the diffusion constants are increased by a factor of ten. To best match the experimental

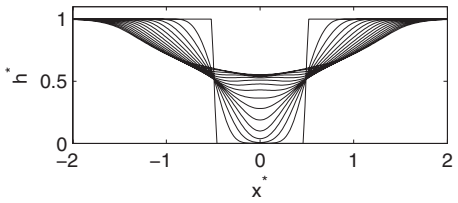

FIG. 11. The free surface of an initially square well, as calculated using the Saint-Venant model, with $f=0.5$ and $D_h^*=D_v^*=0.15$. Profiles are plotted at intervals of 0.1 in Δt^*.

phenomenology, we choose $D_h^*=D_v^*=0.15$. Thus, f, D_h^*, and D_v^* are all constrained by experiment and are not used as fitting parameters.

The evolution of the free surface calculated using this model is shown in Fig. 11. The results are very similar to the experimental data presented in Fig. 5. The depth of the modeled well at $x^*=0$ is plotted as a function of time in Fig. 12 for several values of W^*. As in the experimental system, the filling is reasonably well described by Eq. (4). The quality of the fit is very good for small W^*, but becomes less so for larger W^* as the onset of filling becomes more gradual and the approach to the final depth less exponential. The parameters obtained from these fits are compared with the corresponding experimental results in Fig. 7. Overall, the agreement between experiment and model is good. The time t_{start}^* at which the walls collide, shown as a solid line in Fig. 7(a), increases nearly linearly with increasing W^*, consistent with what is seen experimentally, although the collision of the walls occurs slightly earlier in the model than in the experimental system. The time scale t_{fill}^* associated with the approach to the final depth is plotted in Fig. 7(b). t_{fill}^* increases for $W^* \lesssim 1$, then plateaus for $1 \lesssim W^* \lesssim 2$. Above $W^* \approx 2$, t_{fill}^* increases further, but this is a consequence of the increasingly poor fit of Eq. (4) to the model results, and is not physically meaningful. Experiment and model agree well for most values of W^*. The filling rate y_f^*/t_{fill}^*, shown as a solid line in Fig. 7(c), decreases with W^*, again in good agreement with experiment.

The late-time profiles of the model system, like those of the experimental system, are well described by Eq. (5). The

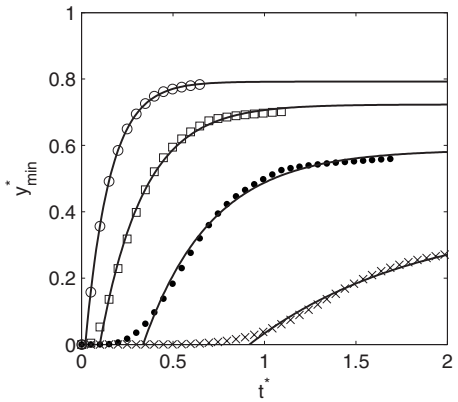

FIG. 12. The depth $y_{\min}^*$ at the center of the collapsing well as a function of t^*, as calculated with the continuum model. ○: $W^*=0.25$, □: $W^*=0.5$, ●: $W^*=1.0$, and ×: $W^*=2.0$. Solid lines are fits to Eq. (4).

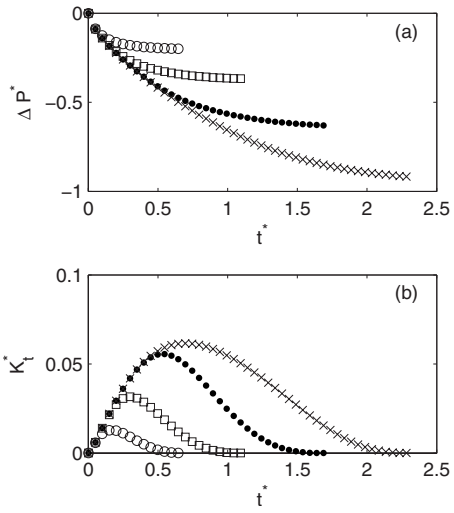

FIG. 13. Energy of the Saint-Venant model. (a) shows the dimensionless potential energy, and (b) the dimensionless kinetic energy, both as a function of dimensionless time. ○: $W^*=0.25$, □: $W^*=0.5$, ●: $W^*=1.0$, and ×: $W^*=2.0$.

dimensionless depth $H_{\rm fit}^*$ obtained from the model is shown as a solid line alongside the experimental data in Fig. 8(a). It shows nearly the same dependence on aspect ratio as the experimental data, including the change in behavior at $W^* \approx 3$, although the model systematically underestimates the depth by about 20%.

The dimensionless model width $2R_{\rm fit}^*$ is shown as a solid line in Fig. 8(b). While the model profiles are 10–30 % wider than their experimental equivalents, both show the same dependence on W^*. The dependence of $R_{\rm fit}^*$ on W^* does not change significantly at $W^* \approx 3$, suggesting that the collision of the walls at the center of the well has little effect on the profile far from the center.

$c_{\rm fit}$, the slope of the model profile, has no significant dependence on W^* and a mean value of $c_{\rm fit}=0.43 \pm 0.05$. This is slightly smaller than the repose slope (and the value of f) measured for the experimental system, likely due to the diffusion terms in Eqs. (6) and (7), which will always drive the system toward a perfectly flat final profile. It is, however, equal within uncertainties to the experimental value of $c_{\rm fit}$ presented above.

The potential and kinetic energies in the Saint-Venant model ΔP^*, and K_t^* respectively, are shown in Fig. 13. The model considers only the depth-averaged velocity, so for simplicity we have assumed when calculating K_t^* that the velocity is constant with depth. ΔP^* and K_t^* are plotted in Fig. 13 and show good qualitative agreement with the experimental results. As in the experimental system, ΔP^* [Fig. 13(a)] decreases smoothly with time. Before the walls collide, ΔP^* is independent of W^*. Following the collision, the rate of change of the potential energy decreases and ΔP^* approaches its final value. Since collisions occur earlier for small W^* than for large, the overall change in potential energy increases with increasing W^*.

As was observed experimentally, the collapse dynamics can be roughly divided into two phases. At early times gravity is dominant and K_t^*, shown in Fig. 13(b), increases. Later,

dissipation dominates and K_t^* decreases. For a square well, the peak in K_t^* occurs at $t^* \approx 0.5$, the same time found in the experimental system. The modeled kinetic energy is independent of W^* at early times, and it starts to decrease following the collision. The level of agreement between these results and the experimental data indicate that the simple depth-averaged model with a constant basal friction represents the dissipation well in this system.

V. DISCRETE ELEMENT MODEL

We also model the collapse of a rectangular well using discrete element simulations [20,37,38,50]. Rather than treating the granular material as a continuous medium, a discrete element model calculates the forces on, and the motion of, each bead individually. We use a "soft-sphere model" where the beads are allowed to effectively deform when they come into contact. We represent particle-particle and particle-wall contact forces using a nonlinear force model in both the normal direction (the direction connecting the centers of two contacting spheres) and the tangential direction (perpendicular to the normal direction and in the direction of relative movement). Both normal and tangential contact force models have a nonlinear elastic component based on Hertzian and Mindlin contact theories and a damping component based on the derivation outlined by Tsuji *et al.* [51] The tangential contact force also obeys the Coulomb friction law. The normal force F_n is calculated as

$$F_n = -k_n \delta_n^{3/2} - \eta_n \delta_n^{1/4} v_n, \tag{8}$$

and the tangential force F_t as

$$F_t = \min\{-k_t \delta_n^{1/2} \delta_t - \eta_t \delta_n^{1/4} v_t, \mu F_n\}. \tag{9}$$

δ_n and δ_t are the effective deformations in the normal and tangential directions, respectively, and are modeled here—as is common practice—as overlap between contacting spheres (see, e.g., Refs. [37,51]). $v_n = d\delta_n/dt$ and $v_t = d\delta_t/dt$. The numerical parameters k_n, k_t, η_n, and η_t are derived from the particle properties as detailed in [51]. We use a density of 2650 kg/m^3, a modulus of elasticity of 29 GPa, a Poisson ratio of 0.15, and a coefficient of friction equal to 0.5. The walls have the same material properties as the particles. The bead diameter was arbitrarily chosen to be 2 mm. The coefficient of restitution of the particles was approximately 0.9, though it varies from one collision to the next depending on the relative particle velocity. Integration is performed using a fourth order Runge-Kutta numerical scheme with a constant time step of $\Delta t^* = 2 \times 10^{-5}$. Simulations using these parameters give a repose slope of 0.4, slightly smaller than that of the experimental system.

Simulations are performed in a virtual Hele-Shaw cell with a gap width of five bead diameters, similar to our experimental system. The simulated cell is sufficiently large that the granular flow experiences no finite-size effects in the x direction. To initialize the system, beads are placed in the cell at a low packing fraction with random initial velocities. The grains are allowed to settle under gravity until all motion stops. At this point, the granular medium has a packing fraction between 0.57 and 0.58, slightly lower than that found in our experimental system. A rectangular well is created by removing the particles in the desired region from the model. In all of our simulations, the depth D of the well is fixed at 12.5 bead diameters.

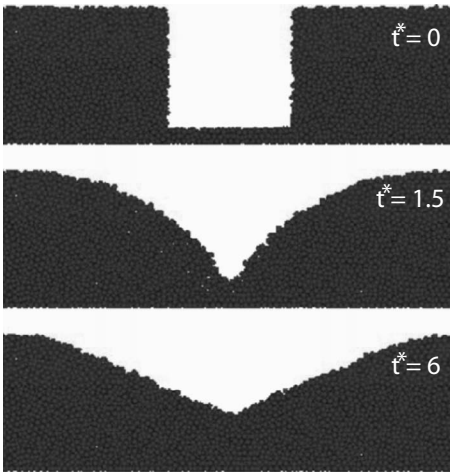

FIG. 14. The collapse of an initially square well, simulated using discrete element methods. In this simulation, $D = W = 25$ mm.

The initial configuration is unstable and immediately starts to collapse. The simulated collapse closely resembles that of the experimental system. Figure 14 shows the configuration of the beads before, during, and after the collapse of an initially square well, and Fig. 15(a) shows the time evolution of the free surface in the same simulation. As above, we fit the depth at the center of the well to an exponential approach to a final depth, Eq. (4). The collision time t^*_{start}, the filling time scale t^*_{fill} and the filling rate y^*_f/t^*_{fill} obtained for the discrete element model are shown as stars in Fig. 7 for three values of W^*, and for the most part agree well with the experimental results. At $W^* = 2$, however, the filling is not well described by Eq. (4), just as was the case for the continuum model at higher aspect ratios. In this case the value of t^*_{fill} is higher than the experimental value and lies just off the top of the graph in Fig. 7(b). At late times, the

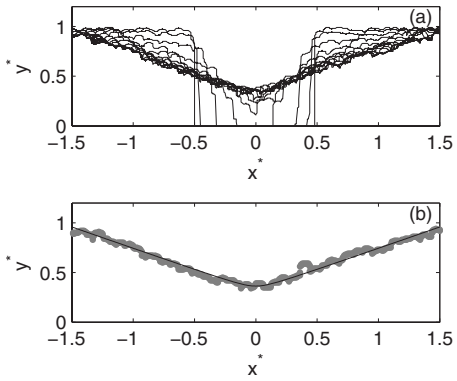

FIG. 15. (a) The evolution of the free surface of an initially square well determined using the discrete element model. Profiles are plotted at intervals of $\Delta t^* = 0.4$. (b) A fit of the late-time profile (gray points) to a hyperbola (solid line) given by Eq. (5). In this simulation, $D = W = 25$ mm.

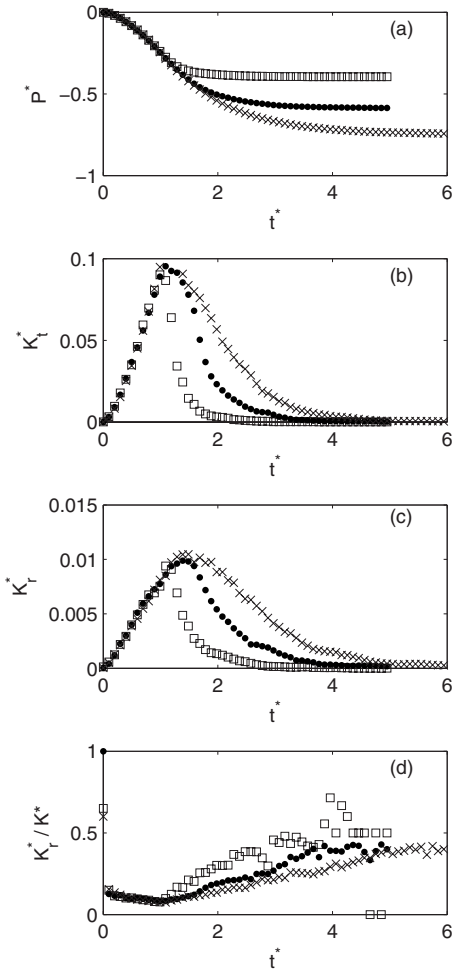

FIG. 16. Energy of the discrete element simulation as a function of dimensionless time. (a) shows the dimensionless potential energy ΔP^*, (b) the dimensionless translational kinetic energy K_t^*, (c) the dimensionless rotational kinetic energy K_r^*, and (d) the rotational kinetic energy as a fraction of the total kinetic energy. In all plots, □ are $W^*=0.5$, ● are $W^*=1.0$ and × are $W^*=2.0$.

simulated profile can be described well by a hyperbola, shown as a bold line in Fig. 15(b). The depth and width of the simulated late-time profiles, extracted from fits to Eq. (5), are shown as stars in Fig. 8 for three values of W^*, and again agree well with both the experimental results and the results from the Saint-Venant model.

The potential energy of the simulated well is shown in Fig. 16(a) for several values of W^*. The results are qualitatively similar to those found for the experimental system, shown in Fig. 10(a), and from the Saint-Venant model, shown in Fig. 13(a). At early times, the evolution of the potential energy is independent of W^*, but diverges from this common behavior when the collapsing walls collide. After the collision, the potential energy of the system smoothly approaches a final value. Since the discrete element simulations have a slightly smaller repose slope, the late-time profiles predicted by this model are flatter and the net change in potential energy is larger.

In both the experiment and Saint-Venant model, we can only determine the kinetic energy associated with the translation of the granular medium. Friction between beads will cause them to rotate, and this rotation will also contribute an amount K_r^* to the total kinetic energy K^* of the system. The discrete element model allows both the translational and rotational kinetic energies to be calculated directly. These quantities are plotted in Figs. 16(b) and 16(c), respectively. The translational kinetic energy found in the discrete element model increases at early times, then peaks and decreases as dissipation becomes more important, approaching zero at late times. This agrees with the results of both the experiment and the continuum model. K_r^* behaves similarly, and both K_r^* and K_t^* reach their maximum values at roughly the time at which the collapsing walls collide, although for larger aspect ratios K_r^* appears to peak later than K_t^*. The fraction of the total kinetic energy due to rotation is plotted in Fig. 16(d). Both contributions to the kinetic energy increase in nearly the same manner during the gravity-dominated phase of the collapse, during which K_r^*/K^* is roughly constant and equal to approximately 0.1. At later times, when the flowing layer is thinner, the rotational kinetic energy becomes relatively more important and K_r^*/K^* increases to roughly 0.5. At very late times this ratio again becomes nearly constant. K_r^*/K^* is only weakly dependent on W^*.

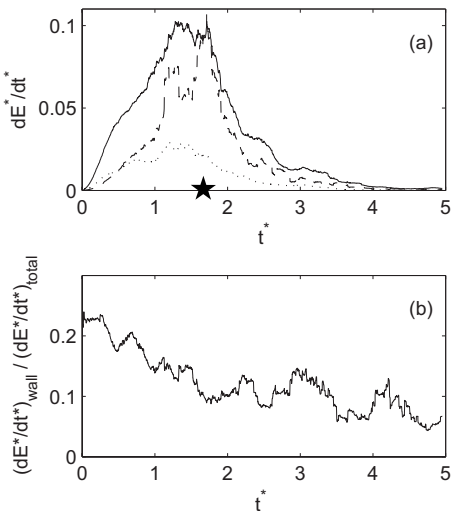

FIG. 17. The rate of energy dissipation during the collapse of an initially square well obtained from the discrete element model. All data have been smoothed using a running average with a width of 0.25 dimensionless time units. (a) shows the dimensionless dissipation rate as a function of t^* for interparticle friction (solid line), inelastic collisions between particles (dashed line), and all particle-wall interactions (dotted line). The approximate time when the walls collide is marked by a star. (b) shows the rate of dissipation due to wall effects as a fraction of the total dissipation rate.

In the Saint-Venant model, dissipation was characterized by a single parameter f. In contrast, the discrete element model allows us to determine the energy dissipated by several different processes. Figure 17(a) shows the rate of energy dissipation due to three major sources: friction between the beads, inelastic collisions between beads, and interactions (collisions and friction) with the wall. We find that friction between particles is the largest source of dissipation at all stages of the collapse. The energy lost through inelastic

collisions is less important at early times, but becomes comparable to frictional losses at intermediate times, approximately when the walls collide. The dissipation rate due to collisions shows a pronounced peak when the walls collide, at which time there is a dramatic spike in the number of collisions. Figure 17(b) shows $(dE^*/dt^*)_{wall}/(dE^*/dt^*)_{total}$, the rate of energy loss due to particle-wall interactions as a fraction of the total dissipation. Particle-wall interactions account for roughly 20% of the energy dissipation at early times, but less than 10% at late times. Cumulatively, friction between particles accounts for roughly 50% of the total energy dissipated during the collapse of an initially square well; inelastic collisions, 35%; and interactions with the walls, 15%. The values will likely depend on material properties; for example the relative importance of damping associated with inelastic collisions would likely increase for particles with a lower coefficient of restitution.

VI. DISCUSSION

Our experimental results on the collapse of a single granular step are consistent with previous work [1–6]. In the case of a collapsing well, the flow changes when the two collapsing steps collide. Nonetheless the shape of the free surface profile once the flow has stopped is well described by a hyperbola in both cases. We previously showed that impact craters in granular materials had the same shape [26]. This similarity suggests that the shape of the crater in the latter case is largely determined by the collapse of transient cavity excavated by the impact, and not by the details of the impact itself. This is consistent with the present understanding of planetary impact crater formation [34]. We also find that the shape of the final profile is independent of the aspect ratio of the initial well. This is disappointing if one was hoping to work backward from the final shape of a crater to determine information about its formation (although we will show elsewhere that the situation is different in three dimensions [52]), but can be explained by simple geometry. If we assume that the sides of an initially rectangular well collapse to form linear slopes at the angle of repose, then it is straightforward to show that the walls collide if $W^* \leq 1/c$ and that both the width and the depth of the final cavity scale like $W^{*1/2}$, so that their ratio is independent of the aspect ratio of the original well. Our experimental results gave power-law exponents very slightly higher than the predicted value of 1/2. On the other hand, the experimental value of the repose slope was $c=0.5$, but collision occurs for $W^* \leq 3$. This is due to the extended "reach" of the curved tail of the profile.

Both of the theoretical models used in this work do a reasonably good job of reproducing the experimentally observed behavior. The continuum model described by Eqs. (6) and (7) is very simple, being based only on conservation of mass and momentum. Since it includes only depth-averaged quantities, it cannot model presence of a flowing layer moving above an underlying static layer, nor the exchange of particles between the layers, as is done explicitly in the BCRE model of Ref. [53]. In addition, the applicability of this model in the early stages of the collapse flow can be questioned, due to the presence of significant vertical velocities. Our model also uses a single, constant parameter f to model all dissipative processes, rather than a more complex granular rheology [9–12]. In the light of these approximations, the semiquantitative agreement between the Saint-Venant model and the experimental results is provocative and somewhat surprising. Similar models have been used successfully in previous models of granular flows [13,19], and a simple basal friction model has been shown to provide a good representation of the results of discrete element simulations [20]. It has been shown that the friction coefficient in a granular flow depends on the inertial number $I=\dot{\gamma}d/\sqrt{P\rho_g}$ [12,54]. Here $\dot{\gamma}$ is the shear rate, d the particle size, P the pressure, and ρ_g the particle density. I can be thought of as the ratio of the time scale for local particle rearrangements to that of the mean flow [12]. Over much of the collapse flows studied here, and particularly at early times, the pressure is likely to be quite low everywhere while the shear rate $\dot{\gamma}$ is significant, so I is expected to be large. The effective friction coefficient has been found to be constant for large I [12,54], which provides an explanation for the success of this approximation here. While one could presumably improve the Saint-Venant model by including a more detailed description of the rheology and the dissipation processes [55,56], Eqs. (6) and (7) arguably constitute the simplest possible model for a granular flow under gravity. The fact that this minimal model can semiquantitatively reproduce the experimentally observed behavior—including the evolution of the free surface, the timing associated with the filling of the well, the time dependence of the kinetic and potential energies, and the shape of the final profile—suggests that while such refinements may provide insight into the detailed physics of the subsurface flow, they are not required to understand the basic phenomena and the shape of the free surface. This also suggests that most of the experimental dynamics result simply from a competition between gravity and dissipation.

On the other hand, there are small quantitative differences between the continuum model and the experimental results, as can be seen in Figs. 7 and 8. The walls collide slightly early in the model, and the model slightly underestimates the depth and overestimates the width of the final cavity. In addition, energy is dissipated faster in the model than in the experiment. These differences are all likely due to the inability of a single friction parameter to reproduce precisely all details of the dissipation in the real system.

The discrete element model gives cavity dimensions that agree quite well with the experimental data, although it also gives collision times that are slightly too high. On the other hand, comparison of the experimental and calculated energies suggests that the discrete element model does a reasonably good job of reproducing the experimental dissipation rate. This model allows a more detailed investigation of the dissipation processes. Our simulations have shown that the translational kinetic energy is initially much larger than that due to rotation, but the rotational kinetic energy due to rotation increases from roughly 10% of the total at early times to over 50% toward the end of the flow. This increase is associated with a qualitative change in the nature of the flow from a thick flow in which grains are largely falling downward under gravity at early times, to a thin flow in which a small number of grains are rolling along an otherwise static

surface at later times. We find that about half of the energy is dissipated through friction between individual grains, although inelastic collisions become more important when the collapsing walls collide and in the later stages of the flow. Wall effects account for only a small fraction of the total energy dissipation.

VII. CONCLUSIONS

We have investigated the collapse under gravity of both a single isolated step and a rectangular well in a quasi-two-dimensional granular medium. For a single step, the collapse dynamics and final configuration scale with the step height D. At early times, each wall of a collapsing rectangular well behaves like an isolated collapsing step. In both cases, the potential energy of the system decreases continuously, while the kinetic energy initially grows, reaches a maximum value, then decays toward zero. This suggests that the early collapse is dominated by gravity while the late collapse is dominated by dissipation processes.

If the rectangular well is sufficiently narrow, the collapsing walls collide and the subsequent dynamics depend on the aspect ratio of the initial well. Following the collision, a region of no flow forms in the center of the well and the well begins to fill. We find that narrow wells fill earlier and faster than wide wells. The time dependence of the kinetic and potential energies is similar to the single-step case, but the approach to the lower potential energy configuration is frustrated by the collision of the walls, and narrow initial wells, colliding early, end up with a higher final potential energy than wider wells.

If the walls do not collide, then the final profile is described by a pair of half-hyperbolae separated by an undisturbed region of the original floor of the well. If they do collide, the final profile is well described by a simple hyperbola. Even though the postcollision dynamics depend on the aspect ratio of the initial well, the final profiles have a self-similar shape that is independent of this aspect ratio. In all cases, the slope of the final profile is equal, within measurement error, to the repose slope of the granular medium.

We modeled the collapse of a rectangular well using a one-dimensional continuum model based on the Saint-Venant equations and a discrete element model. Both models reproduced the experimental behavior well and gave results for the dynamics and the shape of the final profile that agreed semiquantitatively with the experimental results. Given the crudeness of the Saint-Venant model, the good agreement between the model results and the experimental data suggests that both the basic dynamical phenomena and the final shape of the free surface do not depend strongly on the details of the subsurface flow. The discrete element model allowed us to investigate the contributions of friction, inelasticity, and wall interactions to the dissipation of energy in the flow.

ACKNOWLEDGMENTS

This work was supported by NSERC of Canada and the University of Minnesota.

[1] E. Lajeunesse, J. N. Monnier, and G. M. Homsy, Phys. Fluids **17**, 103302 (2005).
[2] N. J. Balmforth and R. R. Kerswell, J. Fluid Mech. **538**, 399 (2005).
[3] S. Siavoshi and A. Kudrolli, Phys. Rev. E **71**, 051302 (2005).
[4] G. Lube, H. E. Huppert, R. S. J. Sparks, and A. Freundt, Phys. Fluids **19**, 043301 (2007).
[5] O. Hungr, Can. Geotech. J. **45**, 1156 (2008).
[6] L. Lacaze, J. C. Phillips, and R. R. Kerswell, Phys. Fluids **20**, 063302 (2008).
[7] O. Pouliquen, Phys. Fluids **11**, 542 (1999).
[8] O. Pouliquen and Y. Forterre, J. Fluid Mech. **453**, 133 (2002).
[9] GDR-MiDi, Eur. Phys. J. E **14**, 341 (2004).
[10] O. Pouliquen, C. Cassar, P. Jop, Y. Forterre, and M. Nicolas, J. Stat. Mech.: Theory Exp. 2006, P07020.
[11] P. Jop, Y. Forterre, and O. Pouliquen, Nature (London) **441**, 727 (2006).
[12] Y. Forterre and O. Pouliquen, Annu. Rev. Fluid Mech. **40**, 1 (2008).
[13] R. R. Kerswell, Phys. Fluids **17**, 057101 (2005).
[14] E. Lajeunesse, A. Mangeney-Castelnau, and J. P. Vilotte, Phys. Fluids **16**, 2371 (2004).
[15] G. Lube, H. E. Huppert, R. S. J. Sparks, and M. A. Hallworth, J. Fluid Mech. **508**, 175 (2004).
[16] G. Lube, H. E. Huppert, R. S. J. Sparks, and A. Freundt, Phys. Rev. E **72**, 041301 (2005).
[17] E. L. Thompson and H. E. Huppert, J. Fluid Mech. **575**, 177 (2007).
[18] T. Boutreux and P.-G. de Gennes, C. R. Acad. Sci. Ser. IIb. Mec. Phys. Astron. **325**, 85 (1997).
[19] A. Mangeney-Castelnau, F. Bouchut, J. P. Vilotte, E. Lajeunesse, A. Aubertin, and M. Pirulli, J. Geophys. Res. **110**, B09103 (2005).
[20] L. Staron and E. J. Hinch, J. Fluid Mech. **545**, 1 (2005).
[21] R. Zenit, Phys. Fluids **17**, 031703 (2005).
[22] L. Lacaze and R. R. Kerswell, Phys. Rev. Lett. **102**, 108305 (2009).
[23] G. B. Crosta, S. Imposimato, and D. Roddeman, J. Geophys. Res. **114**, F03020 (2009).
[24] A. M. Walsh, K. E. Holloway, P. Habdas, and J. R. de Bruyn, Phys. Rev. Lett. **91**, 104301 (2003).
[25] J. R. de Bruyn and A. M. Walsh, Can. J. Phys. **82**, 439 (2004).
[26] S. J. de Vet and J. R. de Bruyn, Phys. Rev. E **76**, 041306 (2007).
[27] J. S. Uehara, M. A. Ambroso, R. P. Ojha, and D. J. Durian, Phys. Rev. Lett. **90**, 194301 (2003).
[28] K. A. Newhall and D. J. Durian, Phys. Rev. E **68**, 060301 (2003).
[29] Z.-J. Zheng, Z.-T. Wang, and Z.-G. Qiu, Eur. Phys. J. E **13**, 321 (2004).

[30] D. Lohse, R. Bergmann, R. Mikkelsen, C. Zeilstra, D. van der Meer, M. Versluis, K. van der Weele, M. van der Hoef, and H. Kuipers, Phys. Rev. Lett. **93**, 198003 (2004).
[31] M. A. Ambroso, C. R. Santore, A. R. Abate, and D. J. Durian, Phys. Rev. E **71**, 051305 (2005).
[32] H. Katsuragi and D. Durian, Nat. Phys. **3**, 420 (2007).
[33] S. Deboeuf, P. Gondret, and M. Rabaud, Phys. Rev. E **79**, 041306 (2009).
[34] H. J. Melosh and B. A. Ivanov, Annu. Rev. Earth Planet Sci. **27**, 385 (1999).
[35] R. M. Lueptow, A. Akonur, and T. Shinbrot, Exp. Fluids **28**, 183 (2000).
[36] S. B. Savage and K. Hutter, J. Fluid Mech. **199**, 177 (1989).
[37] P. Cundall and O. Strack, Geotechnique **29**, 47 (1979).
[38] K. M. Hill and J. Zhang, Phys. Rev. E **77**, 061303 (2008).
[39] Dragonite Grinding Beads, Jaygo Inc., Union, NJ.
[40] M. A. Carrigy, Sedimentology **14**, 147 (1970).
[41] C. H. Liu, H. M. Jaeger, and S. R. Nagel, Phys. Rev. A **43**, 7091 (1991).
[42] S. C. du Pont, P. Gondret, and M. Rabaud, EPL **61**, 492 (2003).
[43] N. Taberlet, P. Richard, A. Valance, W. Losert, J. M. Pasini, J. T. Jenkins, and R. Delannay, Phys. Rev. Lett. **91**, 264301 (2003).
[44] J. E. Maneval, K. M. Hill, B. E. Smith, A. Caprihan, and E. Fukushima, Granular Matter **7**, 199 (2005).
[45] H. Maleki, F. Ebrahimi, and E. N. Oskoee, J. Stat. Mech.: Theory Exp. 2008, P04026.
[46] R. L. Brown and J. C. Richards, *Principles of Powder Mechanics* (Pergamon Press, New York, 1970).
[47] J. K. Sveen, " An introduction to matpiv v.1.6.1," Eprint no. 2, **ISSN** 0809–4403, Dept. of Mathematics, University of Oslo (2004), http://www.math.uio.no/~jks/matpiv
[48] S. T. Thoroddsen and A. Q. Shen, Phys. Fluids **13**, 4 (2001).
[49] V. V. R. Natarajan, M. L. Hunt, and E. D. Taylor, J. Fluid Mech. **304**, 1 (1995).
[50] B. Yohannes, Master's thesis, University of Minnesota, 2008.
[51] Y. Tsuji, T. Tanka, and T. Ishida, Powder Technol. **71**, 239 (1992).
[52] S. de Vet, Ph.D. thesis, University of Western Ontario, 2009.
[53] J.-P. Bouchaud, M. E. Cates, J. R. Prakash, and S. F. Edwards, Phys. Rev. Lett. **74**, 1982 (1995).
[54] F. da Cruz, S. Emam, M. Prochnow, J. N. Roux, and F. Chevoir, Phys. Rev. E **72**, 021309 (2005).
[55] O. Pouliquen and J. W. Vallance, Chaos **9**, 621 (1999).
[56] J. M. N. T. Gray and C. Ancey, J. Fluid Mech. **629**, 387 (2009).